

- [1] A. C. Kak, M. Slaney, *Classics in Appl. Math.* **2001**, 33.
- [2] E. Maire, L. Babout, J. Y. Buffiere, R. Fougères. *Mater. Sci. Eng.* **2001**, A319-321, 216.
- [3] A. Rodríguez, S. A. Sánchez., J. Narciso, E. Louis, F. Rodríguez-Reinoso. *J. Mater. Sci.* **2005**, 40, 2519.
- [4] Y. Anguy, D. Bernard, R. Ehrlich, *Adv. Wat. Res.* **2001**, 24, 913.
- [5] C. Noiriél, P. Gouze, D. Bernard, *Geophy. Res. Let.* **2004**, 31 (24): Art. No. L24603.
- [6] C. Garcia-Cordovilla, E. Louis, J. Narciso. *Overview No. 134, Acta Mater.* **1999**, 47, 4461-4479.
- [7] A. Rodríguez-Guerrero, S. A. Sánchez., J. Narciso, E. Louis, F. Rodríguez-Reinoso. *Acta Mater.* **2006**, 54, 1821.
- [8] A. Rodríguez, E. Louis, J. Narciso, F. Rodríguez-Reinoso. *AEMAC Mater. Compuestos* **2005**, 9-17.
- [9] K. K. Chawla, *Compos. Mater.* Springer-Verlag **2001**, 310-315.
- [10] L. Salvo, P. Cloetens, E. Maire, S. Zabler, J. J. Blandin, J. Y. Buffiere, W. Ludwig, E. Boller, D. Bellet, C. Jossiond. *Nucl. Instrum. Methods. Phys. Res.* **2003**, B 200, 273.

DOI: 10.1002/adem.200600033

## Analysis of Tomography Images of Bonded Fibre Networks to Measure Distributions of Fibre Segment Length and Fibre Orientation\*\*

By J. C. Tan, J. A. Elliott and T. W. Clyne\*

Computed X-ray microtomography is now a well-developed method for studying the three-dimensional structures of porous materials, such as foams<sup>[1-5]</sup> and to a limited extent, some fibrous materials.<sup>[6-8]</sup> Recent advances in the develop-

ment of desktop microtomography machines have further led to their widespread application in materials science research.<sup>[9]</sup> State-of-the-art desktop machines have resolution down to a few microns, making them well-suited for examining structures found in many porous materials. In addition, with the availability of standard visualisation software, generation of tomographic reconstructions from raw data is now a fairly straightforward procedure. However, most commercial packages still have limited capabilities for extracting quantitative data characterising the structure.

There is increasing interest<sup>[6,10-14]</sup> in materials made by bonding together slender metallic members, such as fibres, wires, rods, ribbons etc. This can be done by brazing, sintering, welding or adhesive bonding. An illustrative fibre architecture produced via solid-state sintering is shown in Figure 1. Such network materials typically have high porosity levels, ranging from 40 to 90%. The high surface-to-mass ratio, coupled with the relatively good environmental stability of metals, means they can be attractive in terms of transport phenomena characteristics, leading to applications involving heat transfer, filtration, catalyst support, acoustic damping etc. However, since bonded fibre networks are rarely isotropic,<sup>[6]</sup> systematic quantitative study of the network architecture is crucial for controlling and predicting their mechanical and transport properties. To do this, it is important to be able to extract geometrical data, such as the distributions of length and orientation of fibre segments, from tomographic reconstructions. This paper presents a systematic approach to obtaining this kind of information, using a 3-D skeletonisation technique.

*X-ray Microtomography of Bonded Fibre Networks:* A typical X-ray absorption radiograph is shown in Figure 2(a). Four hundred such radiographs, taken at incremental angles, were used to reconstruct 2-D slices (cross-sections) at different heights. The reconstructed slices are in greyscale, with intensity levels ranging from 0 to 255. The fibres appear as black (intensity of 0) and void as white (intensity of 255). One such slice, for network A material, is depicted in Figure 2(b). However, because of noise and variations in intensity, the fibre cannot be easily identified from this image. In this case, image processing via anisotropic diffusion smoothing<sup>[15]</sup> was first performed to sharpen the fibre edges (Fig. 2(c)), followed by

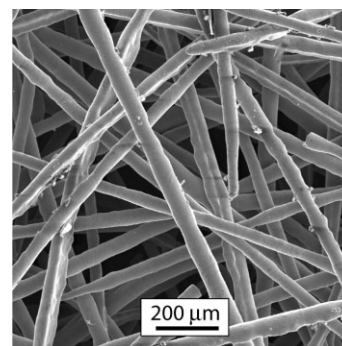


Fig. 1. SEM micrograph of a bonded stainless steel (446) fibre assembly, produced by solid-state sintering.

[\*] Prof. T. W. Clyne, Dr. J. C. Tan, Dr. J. A. Elliott  
Department of Materials Science and Metallurgy  
University of Cambridge  
Pembroke Street, Cambridge CB2 3QZ, U.K.  
E-mail: twc10@cam.ac.uk

[\*\*] One of the authors (JCT) gratefully acknowledges the research funding provided by the Schlumberger & Malaysian Commonwealth Scholarship, ORS Awards, TWI and Cambridge-MIT Institute (CMI).

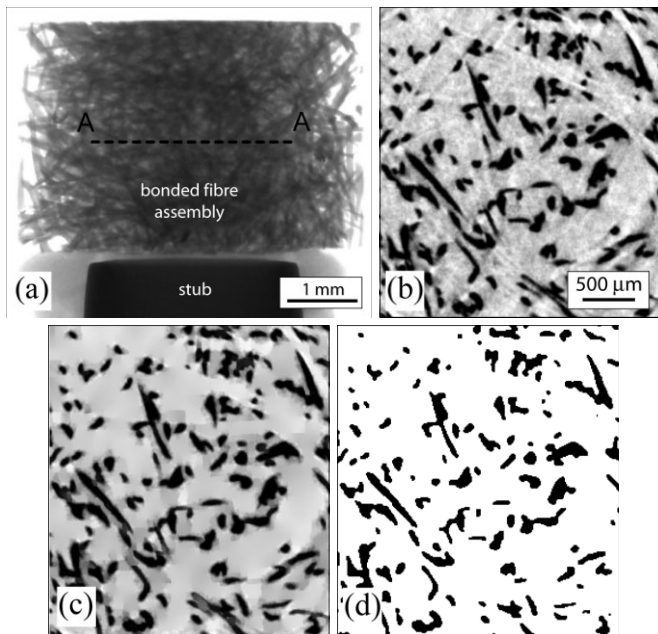


Fig. 2. A typical X-ray absorption radiograph of network A material, (b) a reconstructed 2-D slice through position A-A, (c) the greyscale image after anisotropic diffusion smoothing, and (d) the segmented slice after simple thresholding.

segmentation using simple thresholding (Fig. 2(d)). The segmented images were later used to generate 3-D reconstructions of the network assemblies, as shown in Figure 3. They provide a complete visual impression of the network. Standard software allows the structure to be viewed during rotation about selected axes. Naturally, it can be seen that the bonded networks have complex architecture, containing tortuous fibre segments and many fibre-to-fibre bonds (sintering joints).

**Three-Dimensional Skeletonisation:** In order to extract geometrical statistics from the 3-D fibre networks as shown in Figure 3, the reconstructed fibre surfaces were first simplified to their medial axes or 'skeletons'. The medial-axis offers a skeletal representation of the surface, while preserving its original topology and geometry, so that the network geometry can be efficiently analysed. Details of the skeletonisation algorithm used in this work can be found in.<sup>[8,16–18]</sup> Only a brief overview of the technique, and relevant terminology, will be presented here.

For a digitised fibre network in 3-D space, the medial axis consists of a network of tortuous 'paths' and 'clusters' (Fig. 4). A 'path' is defined as a connected string of filled voxels (3-D pixels), each voxel having exactly two filled neighbours. A 'cluster' is defined as a set of medial axis voxels, each with at least three neighbours lying in the same cluster. Therefore, in the actual fibre network, paths correspond to fibre segments, while clusters correspond to fibre bonds. The number of paths meeting at a cluster is termed the 'coordination number'. Each path on the medial axis can be classified as one of three types:

(a) 'branch-branch' (B-B) path, connecting to a cluster at each end;

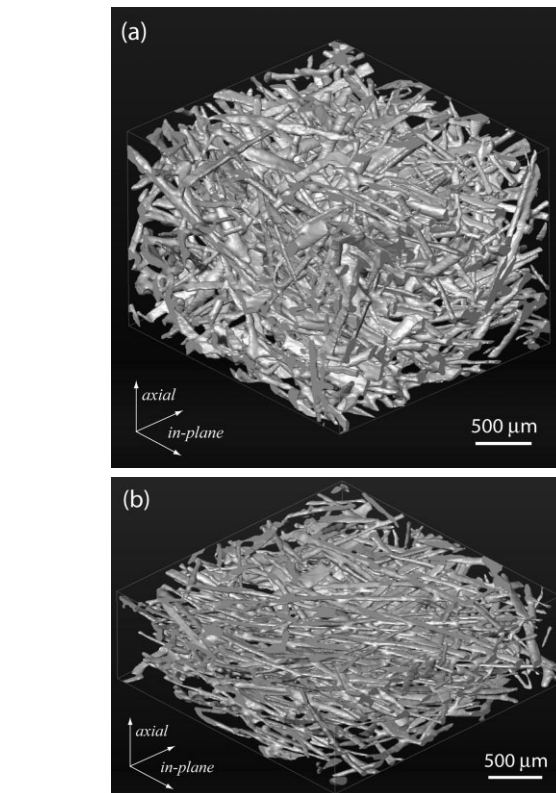


Fig. 3. Three-dimensional tomographic reconstructions of the two types bonded fibre networks being investigated: (a) network A and (b) network B.

(b) 'branch-leaf' (B-L) path, connecting to a cluster only at one end, the other end being free;

(c) 'leaf-leaf' (L-L) path, representing an isolated fibre.

Special precautions were taken to optimise the statistical reliability of the medial axis data. Due to finite volume discretisation, the skeletonisation algorithm generates a number of spurious B-B paths. For two fibres lying across and touching each other (Fig. 4(a)), the 'cluster-merge algorithm' was used to join the two close clusters (with a coordination number 3), to produce a single coordination number 4 branch cluster. When two fibres were crossing at a very acute angle, the medial axis appeared as ladder-shaped and contained a large number of spurious B-B paths. In this case, the 'surface remnant reduction algorithm' was employed to delete the additional paths, leaving behind only the connecting route at the centre of mass of the cluster. Moreover, surface noise (irregularities in the digitised surface) may resemble dead-end fibre segments, hence producing spurious B-L paths. These were eliminated by specifying a user-defined B-L segment length threshold of 100 μm. Also, L-L paths were not taken into account for the statistics, since they could have formed part of longer fibres exiting the imaged region.

Figure 5 shows the 3-D medial axes of network A. Medial axis modification algorithms discussed above were applied to remove spurious B-B segments and to exclude all L-L segments. It can be seen that the medial axes display a clear relationship to the original fibre surfaces.

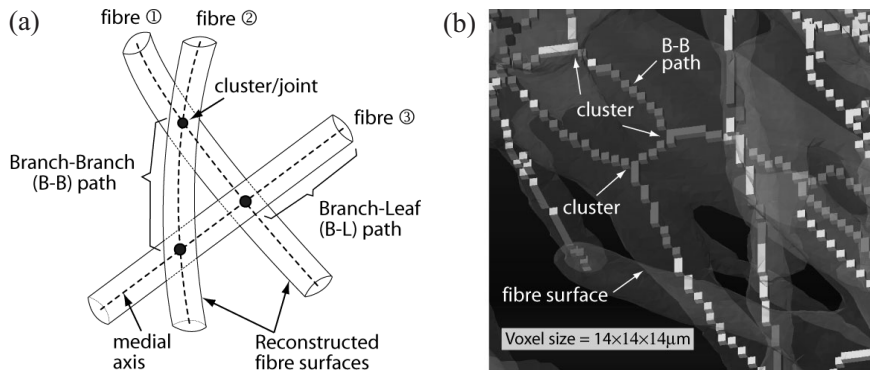


Fig. 4. (a) A schematic depiction of medial axes, paths (fibre segments) and clusters (fibre bonds) formed between three fibres that are in contact. (b) Medial axes (inter-connected voxels) as obtained using the 3-D skeletonisation algorithm. The colour of the voxels designates the closest distance from the medial axes to the reconstructed fibre surface, blue being the furthest away while red being the closest.

**Quantitative Analysis of Fibre Architecture: Fibre Segment Length Distribution:** Using the modified medial axes, such as that depicted in Figure 5, the fibre segment lengths were obtained by extracting the lengths of medial axis paths (voxel strings) connecting any two clusters. The statistics collected come from the branch-branch (B-B) paths. Paths of lengths less than 100  $\mu\text{m}$  were most likely artefacts generated by digitisation noise and were therefore disregarded. Figure 6 presents the segment length distributions of networks A and B. Clearly, both assemblies have a similar distribution, exhibiting a higher probability of finding shorter fibre segments (200–300  $\mu\text{m}$ ) compared with longer ones. Mean segment lengths ( $L$ ) of network A and B were found to be 450  $\mu\text{m}$  and 540  $\mu\text{m}$ , respectively. Taking the mean diameter ( $D$ ) of fibre as  $\sim 60 \mu\text{m}$ , their mean fibre segment aspect ratios ( $L/D$ ) are therefore about 7.5 and 9, respectively.

In general, segment length tends to increase with decreasing (original) fibre length and with decreasing fibre volume fraction. Such an increase is expected as the fibre volume fraction falls, but the effect of fibre length is less easy to predict. However, longer fibres might be expected to favour more entanglements, leading to shorter segments. In this study, although both networks are of similar fibre length and volume fraction, it appears that network B has a higher mean segment length and aspect ratio. This may be related to its more ‘in-plane’ architecture, see Figure 3(b).

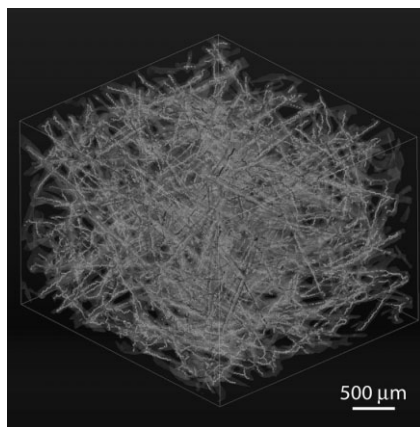


Fig. 5. A skeletonised bonded fibre assembly of network A, superimposed on the original fibre surfaces (shown here in transparent). Clearly, the medial axes preserve the topology and geometry of the fibres (see Fig. 3(a)).

**Fibre Segment Orientation Distribution:** To establish the orientation of fibre segments, the 3-D Medial Axis (3DMA) algorithm<sup>[17]</sup> treats each path as an isolated cylindrical solid body and computes its diagonalised moment of inertia tensor. The three eigenvectors correspond to the principal axes, while the eigenvalues correspond to the moments of inertia about these axes. For a cylindrical body, such as that of a typical fibre

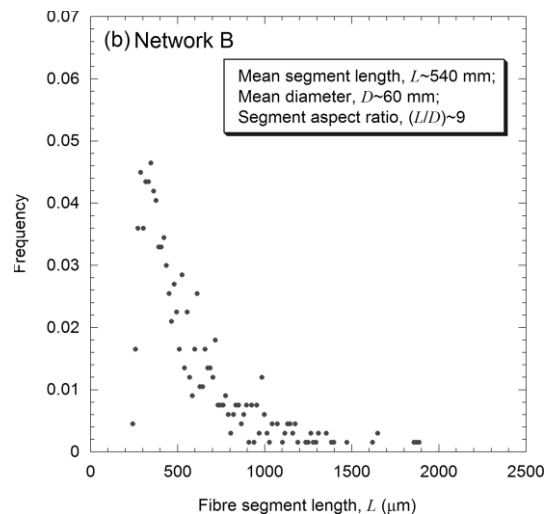
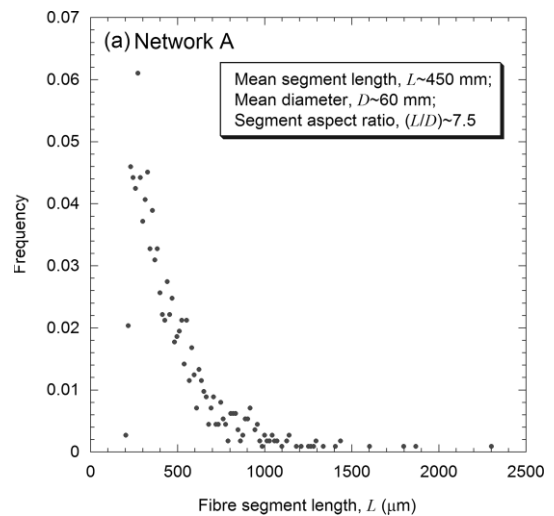


Fig. 6. Fibre segment length (B-B path) distributions for (a) network A and (b) network B materials.

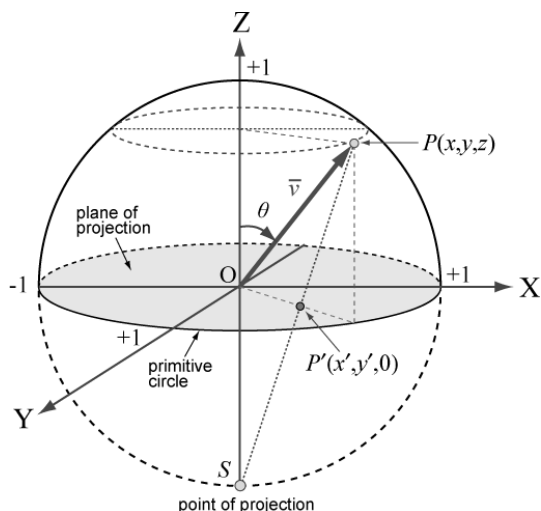


Fig. 7. Schematic illustrating a normalised principle axis,  $\bar{v}$  (a unit vector) and stereographic projection of its tip onto the X-Y plane (projection plane), using the south pole (S) as the point of projection. The fibre segment inclination angle ( $\theta$ ) is measured from the +Z axis.

segment, the larger ( $I_L$ ) and intermediate ( $I_M$ ) moments of inertia will have similar magnitudes, while the smallest moment of inertia ( $I_S$ ) is much lower and corresponds to the fibre axis.

The orientation distribution of fibre segments on the X-Y plane can be represented in the form of a stereographic projection (stereogram), as shown in Figure 7. The use of orthographic projection is not suitable here, since their projections will naturally fall close to the periphery of the primitive circle, creating an impression that most segments lie in-plane. This difficulty can be overcome by using stereographic projection.

In the context of fibre networks, X- and Y-axes denote the in-plane reference directions, while the Z-axis designates the through-thickness (axial) direction. Each directional vector for  $I_S$  was normalised to unit length,  $|\bar{v}|=1$ , and re-plotted from the origin. To convert all unit vectors into the northern hemisphere, the absolute values of Z were taken. Choosing the south pole (S) as the point of projection, the tip of each unit vector was projected onto the projection plane (X-Y plane). The relationship between a point located on the spherical surface,  $P(x, y, z)$ , and that on the X-Y plane,  $P'(x', y', z')$ , can be expressed as:

$$x' = \frac{x}{z+1} ; y' = \frac{y}{z+1} ; z' = 0 \quad (1)$$

The fibre segment inclination angle from the vertical axis,  $\theta$ , is given by:

$$\theta = \sin^{-1} \sqrt{x^2 + y^2} \quad (2)$$

The orientation distribution of fibre segments can also be represented as a frequency plot of inclination angles,  $P(\theta)$ :

$$P\theta = \frac{1}{\Delta\theta_i} \cdot \frac{N_{\theta_i}}{\sum_i^n N_{\theta_i}} \quad (3)$$

where  $N_{\theta_i}$  is the number of segments inclined at an angle  $\theta_i$  (i.e. within a bin of width of  $\Delta\theta_i$ , centred at  $\theta_i$ ). Since the directional vectors were plotted from the origin to the surface of a sphere (Fig. 7), a random distribution (isotropic material) will exhibit a  $P(\theta)=\sin(\theta)$  distribution.

The orientation distributions of networks A and B are presented in Figure 8, using stereograms and frequency plots. The two distributions are clearly very different. Network A is closer to being isotropic, since most fibre segments were found to conform closely to the  $\sin(\theta)$  (random) distribution. The stereogram of network A (Fig. 8(a)) shows projections that are more random. On the contrary, the stereogram of network B (Fig. 8(b)) shows more projections near the periphery of the projection plane, indicating that more fibre segments tend to lie in-plane (large  $\theta$  values). This is also seen in the frequency plot of network B (Fig. 8(d)), where the actual distribution deviates from random distribution and  $P(\theta)$  increases with inclination angle. It is also clear from the stereograms that both distributions are transversely isotropic, as would be expected in view of the manufacturing procedure (see Experimental Procedures).

The fibre distribution data collected via microtomography is particularly useful for predicting the properties of bonded fibre assemblies. A recent example can be found in,<sup>[6]</sup> where the stiffnesses of a transversely isotropic network material in both axial and in-plane directions have been successfully predicted. It is perhaps worth mentioning that this was done using the assumption that the distributions of segment length and segment orientation were independent. A more rigorous analysis would be carried out, in which these distributions were coupled, although this is a more complex procedure. This might be justified in some cases.

**Conclusions:** The following conclusions can be drawn from this work.

- (a) Computed X-ray microtomography is a powerful, non-destructive method to visualise and quantify the architecture of bonded fibre networks.
- (b) By employing a 3-D skeletonisation technique, combined with suitable filtering algorithms, the reconstructed fibre surfaces can be simplified into a medial axis network. Based on this skeletonised network, useful geometrical data, such as the distributions of fibre segment length and orientation can be extracted. This technique is expected to be widely applicable to bonded fibre network materials.
- (c) Fibre segment length distribution can be obtained by extracting the distances of medial axis voxel strings connecting two clusters, which correspond to the distances between two fibre bonds. These values can be used to

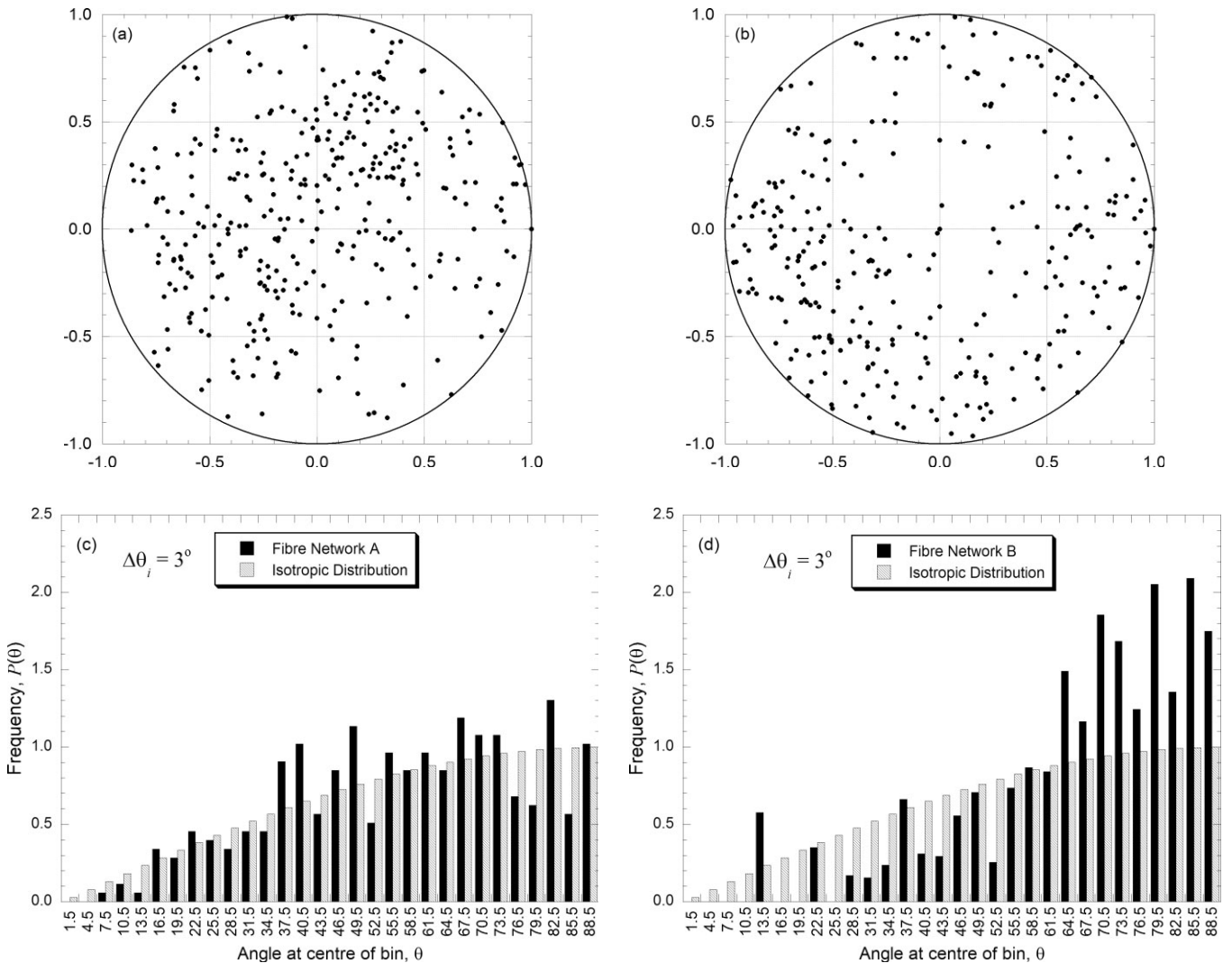


Fig. 8. Orientation distributions of bonded fibre assemblies visualised in Figure 3, depicted as stereograms (projections on X-Y plane) and  $P(\theta)$  frequency plots. Plots (a) and (c) are for network A, while (b) and (d) correspond to network B. The number of fibre segments included in these analyses are respectively about 340 and 300 for networks A and B.

determine the mean segment aspect ratio ( $L/D$ ) of fibre networks.

- (d) Fibre segment orientation distribution was measured by treating each fibre segment as a solid cylindrical body and computing its moment of inertia tensor. The smallest moment of inertia indicates the segment axis. The orientation distribution data can be represented using stereograms and frequency distribution plots, which can be used to evaluate the isotropy of fibre networks.

## Experimental

Two types of bonded fibre network materials were produced, designated as networks A and B, respectively. Both were made from short 446 ferritic stainless steel fibres (Fibretech Ltd), of 60  $\mu\text{m}$  equivalent diameter and 5 mm long. The fibres were loosely packed in a cylindrical glass tube (15 mm diameter) and then gently compressed in the axial direction to obtain the desired fibre volume fraction (~10%) prior to sintering. However, for network B, a higher compressive force was applied during processing to induce a more anisotropic architecture. Both materials were sintered in a tube furnace, under 95% argon and 5% hydrogen atmosphere, at 1200  $^{\circ}\text{C}$ , for about 4 hrs.

Tomography scans were carried out using a high-resolution SkyScan-1072 desktop microtomograph (SkyScan, Belgium), with a spatial resolution of ~5  $\mu\text{m}$ . The cone-beam X-ray source was generated at 100 keV (giving a beam current of 98  $\mu\text{A}$ ). A 1 mm thick aluminium filter was placed in front of the source, to improve the contrast (Fig. 9).

The sintered fibre network materials were cut into  $5 \times 5 \times 5$  mm cubes, using electrical discharge machining (EDM). The sample was then mounted on a stub, which was secured on the stage within the X-ray compartment. During scanning, the sample was rotated, in steps of  $0.45^{\circ}$ , through  $180^{\circ}$ . At each position, an X-ray absorption radiograph was collected, using a  $1024 \times 1024$ , 12 bit CCD camera. The gain and exposure time were set at 1 and 8 sec. respectively. Using these settings, the total scanning time was approximately 1 h per sample.

The complete set of radiographs collected at incremental angles was then used in 3-D reconstruction, employing the Feldkamp algorithm (back-projection algorithm),<sup>[19]</sup> which takes into account convolution and correction for cone-beam. These algorithms are built into the 'Volumetric Reconstruction' software developed by SkyScan.<sup>[20]</sup> 3-D volume reconstruction and rendering were obtained using the AMIRA visualisation package.<sup>[21]</sup> Quantitative analyses were carried out on the tomographic scans, to extract statistical data of fibre segment lengths and orientation distributions. These were done using the 3DMA (3-D Medial Axis) algorithm, developed by Lindquist and co-workers.<sup>[8,16,17]</sup>

Received: January 30, 2006

Final version: February 28, 2006

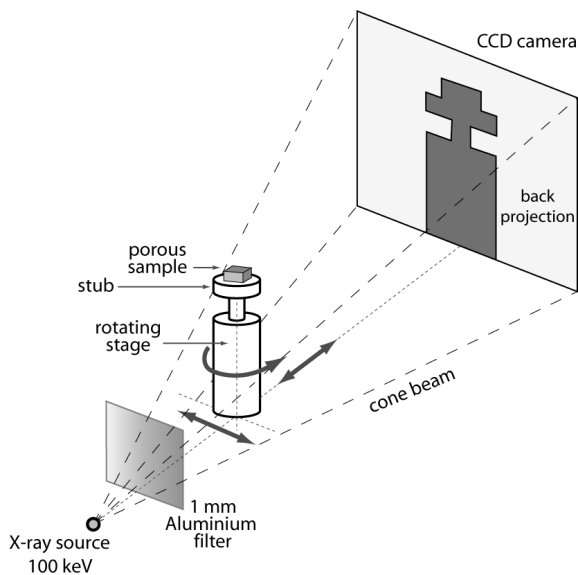


Fig. 9. Schematic of experimental set-up for collecting two-dimensional radiographs of bonded fibre networks, using a cone-beam X-ray arrangement. The set-up resides within an enclosed X-ray compartment.

[16] W. B. Lindquist, A. Venkatarangan, *Phys. and Chem. of the Earth Part A: Solid Earth and Geodesy* **1999**, 24, 593.  
 [17] W. B. Lindquist, *3DMA General Users Manual*, State University of New York at Stony Brook, New York, **1999**.  
 [18] H. Yang, *Department of Appl. Math. and Stat.* State University of New York at Stony Brook, New York, **2001**.  
 [19] L. A. Feldkamp, L. C. Davis, J. W. Kress, *J. Opt. Soc. Am. A* **1984**, 1, 612.  
 [20] Skyscan, <http://www.skyscan.be>, SkyScan, Vluchtenburgstraat 3, B-2630 Aartselaar, Belgium, **2005**.  
 [21] AMIRA, <http://www.amiravis.com>, Mercury Computer Systems, Berlin, **2005**.

DOI: 10.1002/adem.200600042

## Estimation of Elastic Properties of Particle Reinforced Metal-Matrix Composites Based on Tomographic Images\*\*

By Péter Kenesei,\* Horst Biermann and András Borbély

Particle reinforced metal-matrix composites (PMMC) are novel materials often used in industrial applications, however, their mechanical behaviour is not precisely known. Neither elastic nor plastic properties of real MMCs are given accurately by any model, except for those which deal with

[1] J. A. Elliott, A. H. Windle, J. R. Hobdell, G. Eeckhaut, R. J. Oldman, W. Ludwig, E. Boller, P. Cloetens, J. Baruchel, *J. Mater. Sci.* **2002**, 37, 1547.  
 [2] M. D. Montminy, A. R. Tannenbaum, C. W. Macosko, *J. Colloid Interface Sci.* **2004**, 280, 202.  
 [3] E. Maire, A. Fazekas, L. Salvo, R. Dendievel, S. Youssef, P. Cloetens, J. M. Letang, *Comp. Sci. Tech.* **2003**, 63, 2431.  
 [4] A. H. Benouali, L. Froyen, T. Dillard, S. Forest, F. N'Guyen, *J. Mater. Sci.* **2005**, 40, 5801.  
 [5] J. Lambert, I. Cantat, R. Delannay, A. Renault, F. Graner, J. A. Glazier, I. Veretennikov, P. Cloetens, *Colloids Surf. A* **2005**, 263, 295.  
 [6] T. W. Clyne, A. E. Markaki, J. C. Tan, *Comp. Sci. Tech.* **2005**, 65, 2492.  
 [7] M. Faessel, C. Delisee, F. Bos, P. Castera, *Comp. Sci. Tech.* **2005**, 65, 1931.  
 [8] H. Yang, B. W. Lindquist, *Appl. of Digital Image Proc. XXIII, Jul 31-Aug 3 2000*, 4115, Society of Photo-Optical Instrumentation Engineers, Bellingham, WA, USA, San Diego, CA, USA, **2000**, 275.  
 [9] E. Maire, J.-Y. Buffiere, L. Salvo, J. J. Blandin, W. Ludwig, J. M. Letang, *Adv. Eng. Mater.* **2001**, 3, 539.  
 [10] F. Delannay, T. W. Clyne, *MetFoam '99*, Verlag MIT Publishing, Bremen, Germany, **1999**, 293.  
 [11] A. E. Markaki, T. W. Clyne, *Acta Mater.* **2003**, 51, 1341.  
 [12] A. E. Markaki, T. W. Clyne, *Acta Mater.* **2003**, 51, 1351.  
 [13] A. E. Markaki, V. Gergely, A. Cockburn, T. W. Clyne, *Comp. Sci. Tech.* **2003**, 63, 2345.  
 [14] A. E. Markaki, T. W. Clyne, *Encycl. of Mater. Sci. and Technol. – Updates*, Elsevier, **2005**, in press.  
 [15] P. Perona, J. Malik, *IEEE Trans. on Pattern Analysis and Machine Intelligence* **1990**, 12, 629.

[\*] P. Kenesei, Dr. A. Borbély  
 Institute of Physics  
 Eötvös University  
 Budapest, 1518 POB. 32, Hungary  
 E-mail: keno@metal.elte.hu  
 Prof. Dr. H. Biermann  
 Bergakademie  
 Technical University  
 Freiberg 09599, Gustav Zeuner Str. 5, Germany

[\*\*] The authors acknowledge the financial support of the VolkswagenStiftung (grant I/76900). P. K. acknowledges also the support of the Hungarian Science Foundation OTKA under the Grant no. T-043247. A. B. is a grantee of the János Bolyai Scholarship of the Hungarian Academy of Sciences. The authors acknowledge the help of staff of the ID19 beamline at ESRF during measurements and the holotomographic reconstruction.